Engineering Fracture Mechanics 186 (2017) 59–79

Contents lists available at ScienceDirect

Engineering Fracture Mechanics

journal homepage: www.elsevier.com/locate/engfracmech

Modelling of ductile fracture in single point incremental forming using a modified GTN model

Shakir Gatea [a], Hengan Ou [a,*], Bin Lu [b], Graham McCartney [a]

[a] Department of Mechanical, Materials and Manufacturing Engineering, Faculty of Engineering, University of Nottingham, Nottingham NG7 2RD, UK
[b] Institute of Forming Technology and Equipment, Shanghai Jiao Tong University, Shanghai 200030, China

ARTICLE INFO

Article history:
Received 28 July 2017
Received in revised form 15 September 2017
Accepted 17 September 2017
Available online 19 September 2017

Keywords:
GTN damage model
SPIF
Shear mechanism
Finite element method

ABSTRACT

Understanding the deformation and failure mechanisms in single point incremental forming (SPIF) is of great importance for achieving improved formability. Furthermore, there will be added benefits for more in depth evaluation of the effect of localised deformation to the fracture mechanism in SPIF. Although extensive research has been carried out in recent years, questions still remain on the shear and particularly its effect to the formability in SPIF processes. In this work, a modified Gurson–Tvergaard-Needleman (GTN) damage model was developed with the consideration of shear to predict ductile fracture in the SPIF process due to void nucleation and coalescence with results compared with original GTN model in SPIF. A combined approach of experimental testing and SPIF processing was used to validate finite element results of the shear modified Gurson–Tvergaard-Needleman damage model. The results showed that the shear modified GTN model improved the modelling accuracy of fracture over the original GTN model under shear loading conditions. Furthermore, the shear plays a role under meridional tensile stress to accelerate fracture propagation in SPIF processes.

1. Introduction

Single point incremental forming (SPIF) is a relatively new flexible forming process. SPIF process has excellent adaptability to CNC milling machines due to the fact that it does not require the use of high capacity presses or specific dies and it is easy to automate for both symmetric and non-symmetric shapes. In SPIF, a blank sheet is fixed by a holder on a CNC milling machine. A workpiece is formed by the action of a small hemispheric tool in contact with the blank and to move along a user-specified tool path and incrementally deform the blank to a desired shape. Extensive research has been published on SPIF for improved understanding of material deformation and fracture mechanisms of SPIF to form a part without defects. A theoretical model for different modes of deformation in SPIF was built upon membrane analysis and ductile damage mechanics by Martins, Silva and co-workers [1,2]. Experimental observations show that fracture is not preceded by localised necking and cracks develop by tensile meridional stresses under stretching conditions but not by plane shear stresses. An experimental work using a surface 3D digital image correlation showed that the fracture occurred in the uniaxial stretching domain [3].

To predict the occurrence of failure in AA5052 sheet, Malhotra et al. [4,5] used explicit finite element (FE) simulation with a damage-based fracture model, in which the failure envelope was depended on the hydrostatic pressure and the Lode angle. It was noticed that the damage evolution was controlled by local bending around the tool and through-thickness shear. An

* Corresponding author.
E-mail address: h.ou@nottingham.ac.uk (H. Ou).

https://doi.org/10.1016/j.engfracmech.2017.09.021
0013-7944/

experimental and numerical study was undertaken by Xu et al. [6] to investigate the effect of through-thickness shear on AA5052-H32 sheet formability in SPIF. As a result, the fracture depth of the cone produced by SPIF was greater than that of the same cone formed by deep drawing. This result therefore indicates that the through-thickness shear in deep drawing can be disregarded as it is not significant when compared to that obtained from SPIF. To address the established fact of improved formability of SPIF as compared to conventional stamping processes, Allwood et al. [7] gave an explanation for this phenomenon by comparing SPIF with conventional process using paddle forming process with the same geometry. They noted under uniform proportional loading, the forming limit is increased when the through-thickness shear is present. An alternative theory was proposed by Emmens and co-workers to attribute the increased forming limit of SPIF to the deformation of bending-under-tension [8]. Jackson and Allwood [9] used FE simulation to study the effect of through-thickness shear on the formability of SPIF. The results showed that the through-thickness shear could affect the formability due to a significant through-thickness shear occurring in the direction parallel to the tool motion. They demonstrated that the material in the contact zone tends to move in the direction of the tool displacement due to friction.

In micromechanics based approaches in predicting fracture of ductile materials, a comprehensive study was carried out by Bouchard and co-workers in developing Gurson-type models using a mixed velocity-pressure FE formulation to review and clarify the constitutive equations of Avaras and to give proof of the equality of tangent moduli between Zhang and Govindarajan-Avaras [10]. The results showed good accuracy of the analytical formulation and the validity of implementation for a mixed velocity-pressure FE formulation. On the other hand, Tekkaya and co-workers developed an ion beam slope cutting method to prepare the specimen from a notched tensile test for SEM analysis for detailed examination of nucleation and growth of voids during the deformation of dual-phase steel DP600 [11].

A GTN yield criterion was developed utilizing Abaqus/Explicit via a user-defined material subroutine (VUMAT) by Chen and Dong based on the Hill'48 yield model to predict the damage of anisotropic sheet in deep drawing of a cylindrical cup [12]. It was concluded that the Hill'48-GTN plastic yield criterion provided a promising means to predict the plastic behaviour and fracture in sheet metal forming. Kami et al. developed a Hill'48-GTN yield criterion to predict fracture in the deep drawing process of a rectangular box [13] and to construct a forming limit diagram of AA6016-T4 anisotropic sheet [14]. The FE results showed that the GTN model was able to predict fracture and to provide a realistic description of the material response in the whole forming process. Lievers et al. [15] presented a method to determine the void nucleation rate in the SPIF process based on density changes using the GTN model. Three automotive aluminium sheet alloys (AA5754, AA5182 and AA6111) were used to calibrate the void nucleation behaviour. This technique provides a large homogenous deformation area and avoids the large strain and stress gradient associated with smooth or notched tensile specimens. Smith et al. [16] attempted to evaluate the effect of shear on the fracture depth in SPIF process via LS-DYNA explicit software with a shear-modified GTN model proposed by Nahshon and Hutchinson using a partial strip of a full- SPIF model to show an influence on the fracture depth.

It appears from the literature that questions still remain on the shear and particularly its effect to the formability in SPIF processes. Therefore, the main motivation of this study is to develop a GTN based model and to investigate its accuracy and effectiveness in predicting the ductile fracture in SPIF processing of typical truncated cone and pyramid shapes. In the original GTN model, the increment of void volume fraction is measured based on the nucleation and growth of voids. In this study, Nahshon-Hutchinson type shear mechanism was incorporated in GTN model to take into account of the effect of shear in the increment of void volume fraction. The modified GTN model was implemented via Abaqus/explicit to study the effect of shear on the fracture occurrence in SPIF. The FE results obtained from the original GTN model and the shear modified GTN model were validated by SPIF experimental results.

2. Constitutive model (GTN model)

Ductile fracture of metallic materials mostly occurs by the mechanism of nucleation, growth and coalescence of microvoids. A void can be nucleated from an inclusion or second phase particle by decohesion or cracking, and it grows due to the development of localised plastic strain under the application of tensile hydrostatic stresses. The void of material is defined as a ratio of the volume of voids to the total volume of the material. It is denoted by f and also referred to as the void volume fraction (VVF). The shape of the void is assumed to be spherical and it is scattered randomly in the matrix [17]. When the material is fully dense without any void, the f value is 0 or 1 if the material is completely void without any stress carrying capacity. When the space between two adjacent voids is small enough, the voids begin to coalesce and this leads to cracks and subsequent fractures of the material, as shown in Fig. 1 [18,19]. This phenomenon can be analysed utilizing damage models taking into account the effect of microstructure defects by defining a relationship between particular failure stages and the strength of the material.

Gurson's porous metal plasticity model [17], later modified by Tvergaard and Needleman (GTN) [20], is one of the most commonly used material damage models for the prediction of fracture.

Mises theory assumes that the hydrostatic stress component does not affect the yield stress. Whereas ductile fractures in materials are completely due to void growth, e.g. porous materials, these materials harden in compression due to the closing of voids and soften under tension due to void growth, as shown in Fig. 2 [21].

Hydrostatic stress causes dilatancy and influences the yield stress if the ductile fracture depends on void growth, as shown in Fig. 3. With Mises material, $f = 0$, the yield surface is a straight line, which means hydrostatic stress has no effect.

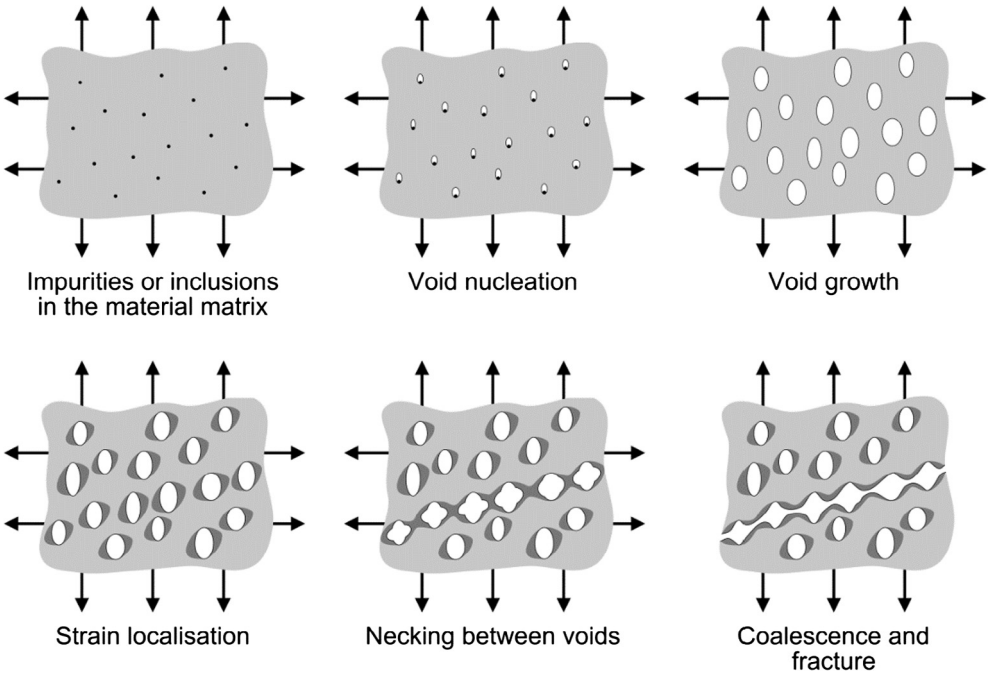

Fig. 1. Schematic of nucleation, growth and coalescence of voids.

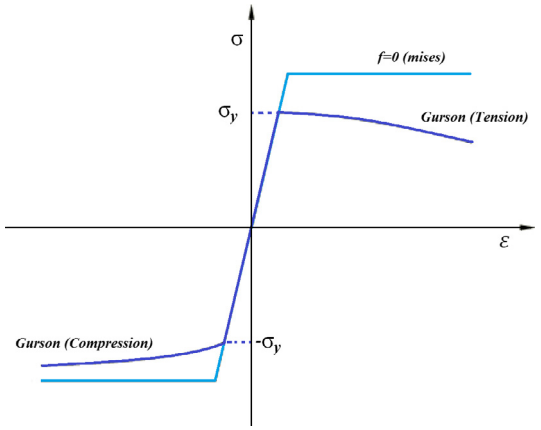

Fig. 2. Comparing uniaxial behaviours of porous metals with Mises materials [21].

However, when the void volume fraction increases, the yield surface gets smaller due to the fact that yielding occurs at lower values of equivalent stress [20,22,23].

The classical plasticity theory (the von Mises theory) was extended by Gurson [17] to cover the effect of plastic dilatancy and pressure sensitivities of inelastic flow based on the observation that the nucleation and growth of voids in a ductile metal can be described macroscopically. The Tvergaad-Needleman modification (GTN model) [20] is considered as one of the most adopted variants of Gurson's original model. This model introduces a void volume fraction f^* and three constitutive coefficients q_1, q_2 and q_3 characterizing the integration effects between voids. The yield function of the GTN model takes the following form:

$$\varnothing = \left(\frac{\sigma_q}{\sigma_y}\right)^2 + 2q_1 f^* \cosh\left(-\frac{3q_2 p}{2\sigma_y}\right) - (1 + q_3 f^{*2}) = 0 \tag{1}$$

where $\varnothing$ is the non-dilatational strain energy; q_1, q_2 and q_3 are the constitutive parameters proposed by Tvergaard [24] to get closer agreement between the GTN model and the full numerical analyses of a periodic array of voids with suggested values of $q_1 = 1.5$, $q_2 = 1.0$ and $q_3 = 2.25$; $\sigma_q = \sqrt{\frac{3}{2} S_{ij} S_{ij}}$ is equivalent to von Mises stress; $S_{ij} = \sigma_{ij} - \frac{1}{3}\sigma_{ii}$ is a deviatoric stress

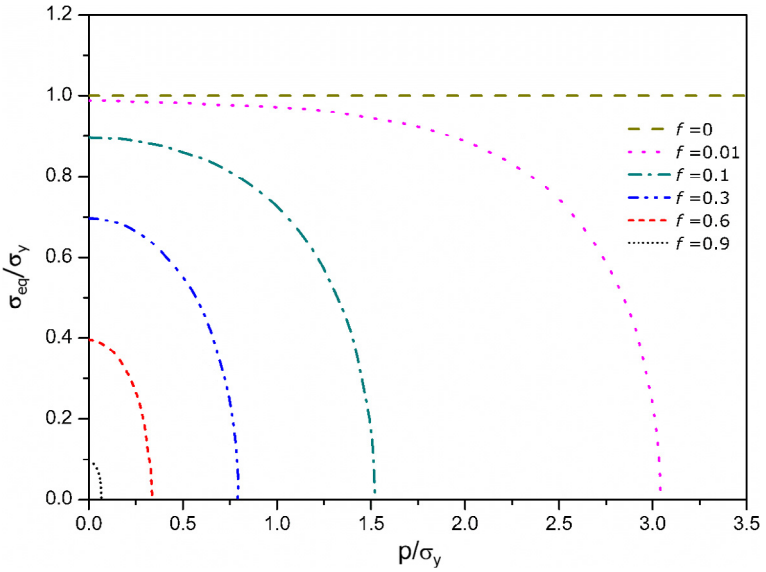

Fig. 3. The dependence of yield surface on the hydrostatic stress for various values of void volume fraction [23].

tensor; $p = -\frac{1}{3}\sigma_{ii}$ is the hydrostatic stress; and σ_y is the flow stress of the undamaged material matrix. The parameter f^* was introduced by Tvergaard-Needleman to account for the final material failure for void coalescence. This parameter is a function of the void volume fraction f and is specified as

$$f^* = \begin{cases} f & \text{if } f \leqslant f_c \\ f_c + \frac{\bar{f}_F - f_c}{f_f - f_c}(f - f_c) & \text{if } f_c < f < f_F \\ \bar{f}_F & \text{if } f \geqslant f_F \end{cases} \tag{2}$$

where f_c denotes the critical value of the void volume fraction, and f_F is the final value of the void volume fraction when the material has completely lost its stress carrying capacity. The function of $\bar{f}_F$ is defined as

$$\bar{f}_F = \frac{q_1 + \sqrt{q_1^2 - q_3}}{q_3} \tag{3}$$

The increase in the initial void volume fraction f is defined as the sum of the increment due to void nucleation and void growth

$$df = df_{nucleation} + df_{growth} \tag{4}$$

The nucleation mechanism is considered to be dependent exclusively on the plastic strain of the matrix material and it is assumed that the voids are nucleated only in tension.

$$df_{nucleation} = A d\bar{\varepsilon}_m^p \tag{5}$$

where

$$A = \begin{cases} \frac{f_N}{S_N\sqrt{2\pi}} e^{-0.5\left(\frac{d\bar{\varepsilon}_m^p - \varepsilon_N}{S_N}\right)^2} & \text{if } p \geqslant 0 \\ 0 & \text{if } p < 0 \end{cases} \tag{6}$$

The parameter A is defined as a function of the matrix of total equivalent plastic strain ε_m^p, f_N is the void volume fraction of the nucleated void; ε_N is the mean value of the normal distribution of the nucleation strain; and S_N is the standard deviation. $d\bar{\varepsilon}_m^p = \frac{\sigma : d\varepsilon^p}{(1-f)\sigma_y}$ is equivalent to plastic strain.

$$df_{growth} = (1 - f) d\varepsilon_{ii}^p \tag{7}$$

where $d\varepsilon_{ii}^p$ is the trace of the plastic strain tensor.

3. Shear mechanism

The GTN model has its limitations as it ignores the fracture mechanism due to shear (low stress triaxiality $\eta = -p/\sigma_q$). A number of papers have been published recently to develop modified GTN models by adding a function to capture the fracture at low stress triaxiality, Xue's shear mechanism [22] and Nahshon-Hutchinson's shear mechanism [25] have received most attention. In this work, Nahshon-Hutchinson's shear mechanism is used because this model showed a good correlation between the FE simulation and experimental tests [25]. In addition, it has shown improved accuracy of fracture over Xue's shear mechanism under tensile/shear loading conditions [26].

Nahshon and Hutchinson introduced an expression used to predict the increase in the rate of void due to low stress triaxiality, which is written as

$$df_{shear} = k_w \frac{f\omega(\sigma)}{\sigma_q} S : \dot{\varepsilon}^p \tag{8}$$

where $\omega(\sigma)$ is a function of the stress state and its value is calculated as:

$$\omega(\sigma) = 1 - \left(\frac{27J_3}{2\sigma_q^3}\right)^2 \tag{9}$$

The value of ω lies in the range of $0 \leqslant \omega \leqslant 1$ with all axisymmetric stress states $\omega = 0$ and for all the states comprised of pure shear plus a hydrostatic contribution $\omega = 1$. k_w is a parameter producing the damage rate in shear loading, and J_3 is the third invariant of the deviatoric stress tensor $J_3 = \det(S)$.

The total void volume fraction after the additional contribution of the shear mechanism thus becomes

$$f_{total} = f_{initial} + (df_{nucleation} + df_{growth} + df_{shear}) \tag{10}$$

4. Implementation of the modified GTN model

The modified GTN model has been implemented in Abaqus/explicit through the material user subroutine VUMAT. This analysis employs the constitutive equation of GTN model to determine whether plastic deformation occurs. The VUMAT subroutine begins by assuming the increment in the strain is purely elastic, and based on this assumption a trial stress is calculated before the yield function is checked. Thus, if $\varnothing \leqslant 0$, the current state is elastic, it is necessary to update the stresses and exit; if not, the current state is plastic and the incremental plastic strain should be determined. Fig. 4 shows the flow chart of the stress integration algorithm of the modified GTN model. In this work, return mapping algorithm is used to compute the increment in plastic strain ($d\bar{\varepsilon}^p$) [27,28] and is briefly summarised below.

The VUMAT begins by assuming the incremental strain is purely elastic and, based on this assumption, a trial stress is calculated. Hook's law is obeyed to determine the trial stress,

$$\sigma_{t+\Delta t}^{trial} = \sigma_t + 2\mu\Delta\varepsilon_{ij}^{el} + \lambda\varepsilon_{ii}^{el}\delta_{ij} \tag{11}$$

where $\sigma_{t+\Delta t}^{trial}$ refers to Cauchy stress tensor, $\mu = \frac{E}{2(1+\nu)}$ is a shear modulus, $\lambda = \frac{E\nu}{(1+\nu)(1-2\nu)}$ is the first Lamé parameter, $\Delta\varepsilon_{ij}^{el}$ is the increment in tensor of elastic strain, ε_{ii}^{el} is the trace of the elastic strain tensor and δ_{ij} is a Kronecker delta (with $\delta_{ij} = 1$, if $i = j$ and $\delta_{ij} = 0$, if $i \neq j$).

The equivalent stress $\left(\sigma_q^{trial}\right)$ is derived from deviatoric components, S_{ij},

$$S_{ij}^{trial} = \sigma_{ij}^{trial} + P \tag{12}$$

where $P = -\frac{\sigma_{ii}^{trial}}{3}\delta_{ij}$ is hydrostatic pressure

$$\sigma_q^{trial} = \sqrt{\frac{3}{2} S_{ij}^{trial} S_{ij}^{trial}} \tag{13}$$

The values of the trial hydrostatic and equivalent stresses are used in the modified GTN model in Eq. (1) to check whether the plastic strain deformation occurs. If the current state is plastic, the incremental plastic strain $\left(d\varepsilon_{ij}^p\right)$ is determined by:

$$d\varepsilon_{ij}^p = \Delta\lambda \frac{\partial \varnothing}{\partial \sigma_{ij}} \tag{14}$$

where $\Delta\lambda$ is the plastic consistency parameter.

The equivalent plastic strain ($d\bar{\varepsilon}^p$) is defined by

$$d\bar{\varepsilon}^p = \sqrt{\frac{2}{3} d\varepsilon_{ij}^p d\varepsilon_{ij}^p} \tag{15}$$

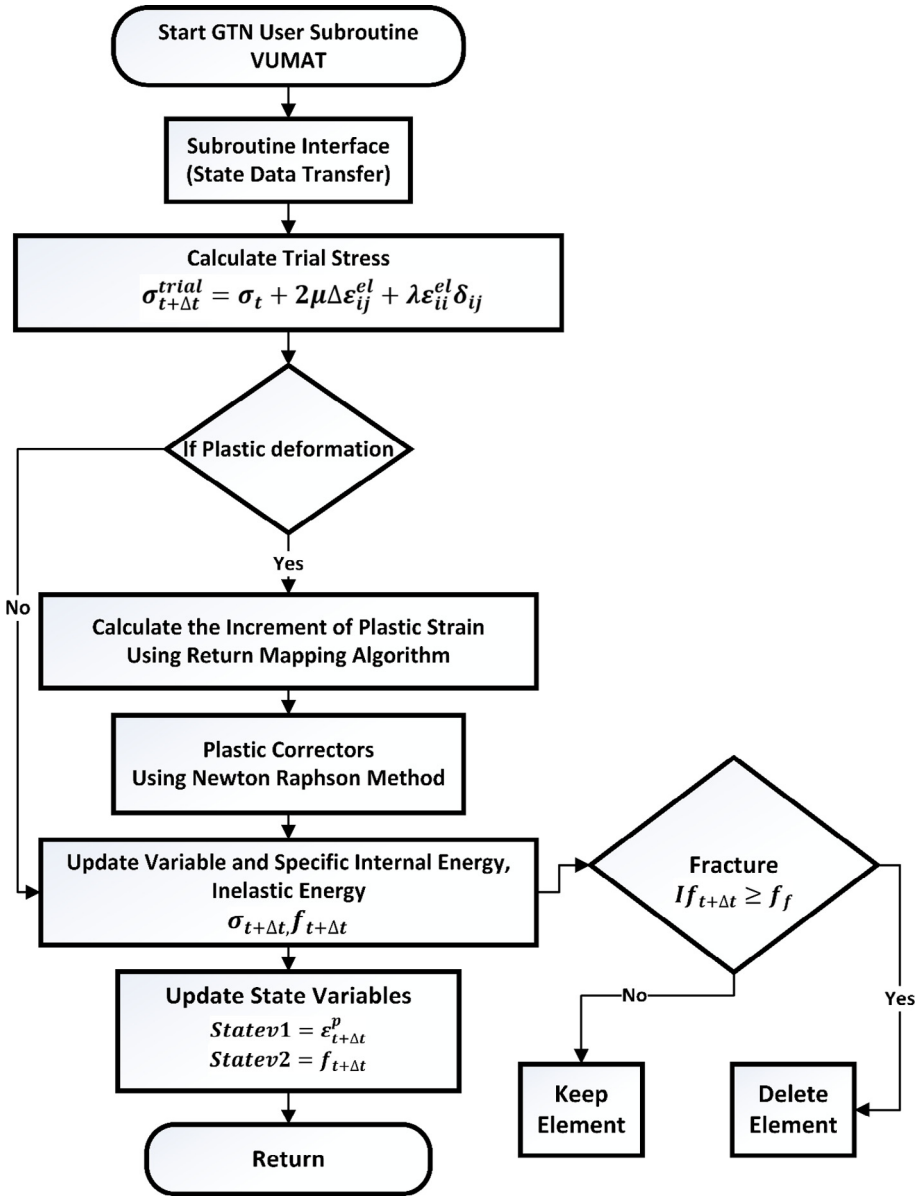

Fig. 4. VUMAT subroutine flowchart of the modified GTN model.

The change in plastic consistency parameter $\Delta\lambda$ is:

$$\Delta\lambda = \frac{\varnothing}{V_{ij}D_{ik}V_{ik} - \xi_1 h_1 - \xi_2 h_2} \tag{16}$$

The definitions of ξ_1, ξ_1 and V_{ik} in terms of stress components are:

$$\xi_1 = \frac{\partial\varnothing}{\partial\bar{\varepsilon}^p} = -\frac{2H}{\sigma_y^3}\left[\frac{3}{2}\sigma_{ij}\sigma_{ij} - 0.5\sigma_{ii}^2\right] - \frac{Hf^* q_1\sigma_{ii}}{\sigma_y^2}\sinh\left(\frac{q_2\sigma_{ii}}{2\sigma_y}\right)\delta_{ij} \tag{17}$$

where $H = \frac{\sigma_y - \sigma_y^{old}}{d\bar{\varepsilon}^p}$ is the tangent of the flow stress, σ_y is initial yield stress, σ_{ij} is the tensor of plastic stress, σ_{ii} is the trace of the stress tensor and f^* is the accumulated of void volume fraction.

$$\xi_2 = \frac{\partial\varnothing}{\partial f} = 2q_1\cosh\left(\frac{q_2\sigma_{ii}}{2\sigma_y}\right) - 2q_3 f^* \tag{18}$$

$$V_{ik} = \frac{\partial \varnothing}{\partial \sigma_{ik}} = \frac{1}{\sigma_y^2}[3\sigma_{ik} - \sigma_{ii}\delta_{ik}] + \frac{f^* q_1 q_2}{\sigma_y} \sinh\left(\frac{q_2 \sigma_{ii}}{2\sigma_y}\right)\delta_{ik} \tag{19}$$

The components of h values are found to be:

$$h_1 = \sqrt{\frac{2}{3} V_{ij} V_{ij}} \tag{20}$$

$$h_2 = (1 - f^*) V_{ii} \tag{21}$$

The elastic constant matrix is defined as:

$$D_{ik} = \begin{bmatrix} 2\mu+\lambda & \lambda & \lambda & 0 & 0 & 0 \\ \lambda & 2\mu+\lambda & \lambda & 0 & 0 & 0 \\ \lambda & \lambda & 2\mu+\lambda & 0 & 0 & 0 \\ 0 & 0 & 0 & \mu & 0 & 0 \\ 0 & 0 & 0 & 0 & \mu & 0 \\ 0 & 0 & 0 & 0 & 0 & \mu \end{bmatrix} \tag{22}$$

After determination of the value of incremental plastic strain ($d\varepsilon_{ij}^{pl}$), this value is used to update the stress and void volume fraction by updating the equivalent plastic strain

$$d\bar{\varepsilon}_m^p = \frac{\sigma : d\varepsilon_{ij}^p}{(1-f)\sigma_y} \tag{23}$$

5. Experimental testing and FE simulation

This section is divided into four parts. The first part summarises the experimental investigation to measure the GTN model parameters of pure titanium sheets using tensile test with scanning electron microscope (SEM). The second part evaluates the mesh size effect in order to accurately predict fracture in FE simulation. The third part presents the validation results of the modified GTN model by using both the tensile and shear tests. Finally, the last part reports the use of the modified GTN model to capture the fracture occurrence in the SPIF process for both a truncated hyperbolic cone and a truncated pyramid.

5.1. Determination of GTN model parameters of pure titanium

In order to simulate the SPIF process by using FEM, the mechanical properties of the sheet metal should be determined. In this work, an INSTRON testing machine was utilized and the specimen design was in accordance with British standard (BS EN 10002-1). Tensile specimens were obtained by using electrical discharge machine (EDM) cutting from 0.7 mm thick grade 1 titanium sheet. The tensile test was carried out at a strain rate of 0.00133 s^{-1}. The reason for choosing grade 1 pure titanium in this study is because it is commonly used in sheet forming of cranioplasty implants. The mechanical properties of the pure titanium are given in Table 1. To measure the displacement on the surface of a specimen during tensile tests, a Dantec Q-400 DIC (digital image correlation) system was used.

To determine material parameters of the developed GTN model, a DIC system was used to measure the deformation and to evaluate necking and fracture along the tensile specimen and a scanning electron microscope was used to obtain the images of the microstructure and to determine the void volume fraction at different stages throughout the tensile test. To evaluate the heterogeneity of deformation and measure the displacement on the surface of the tensile specimen, several tensile tests were carried out. Fig. 5 shows the load displacement curve produced from the tensile test with three different stages identified to determine the GTN model parameters. Fig. 6 illustrates the true strain distribution on the tensile specimen from digital image correlation at nucleation, critical and fracture stages.

In SEM microscopic evaluation, the first step was to determine the primary void volume fraction by scanning the sheet before plastic deformation. The initial void volume fraction came from original voids, non-metallic inclusions and second-phase particles, as shown in Fig. 7(a). These inclusions were randomly distributed in the metal matrix. The initial void volume fraction f = 0.00138 was determined as a mean value of original voids and inclusions. When the tensile specimen is subjected to plastic strain under external loading, the nucleation mechanism is started by void formation around the inclusions

Table 1
Mechanical properties of pure titanium.

Yield stress	Ultimate tensile stress	Young's modulus	Poisson's ratio	Density
232.49 MPa	363 MPa	108 GPa	0.34	4505 kg/m^3

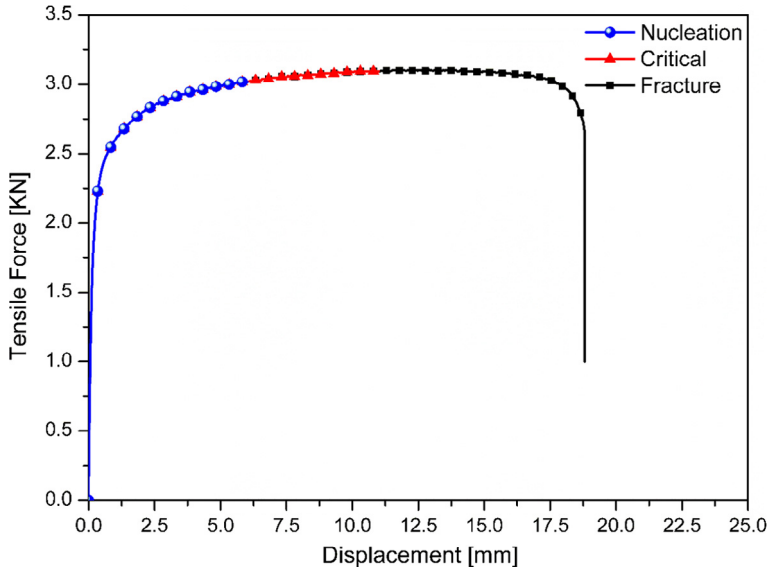

Fig. 5. Load-displacement curve of in tensile test.

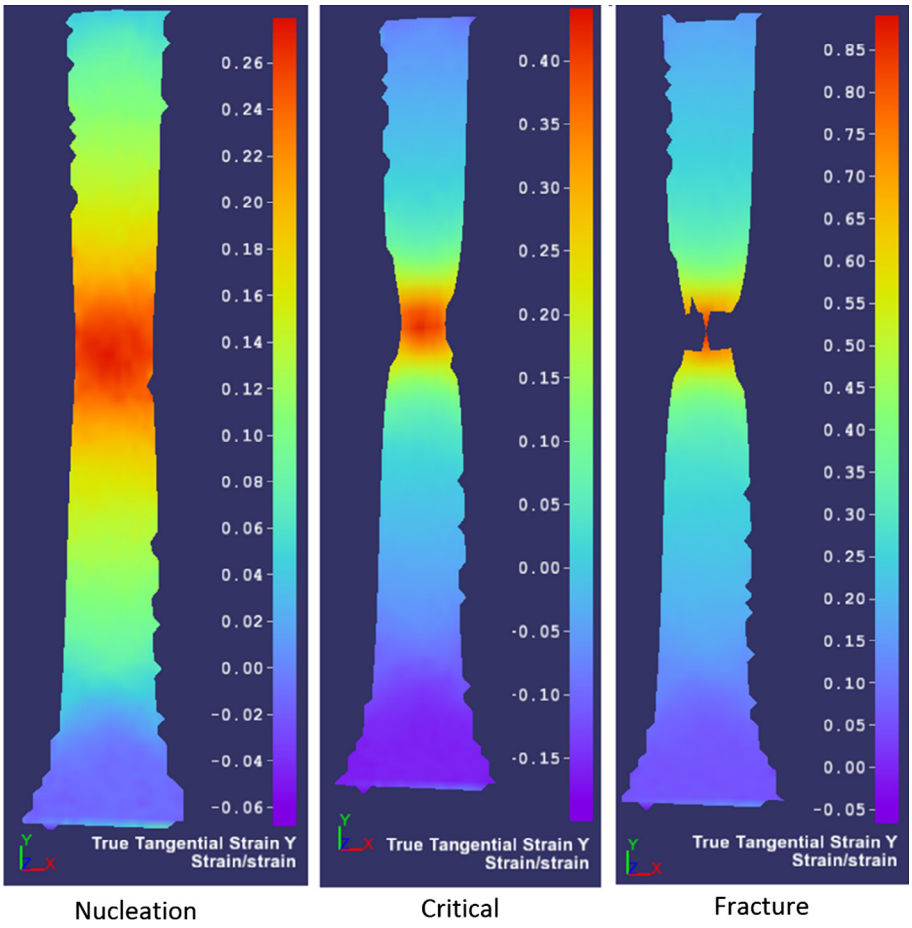

Fig. 6. True strain distribution from digital image correlation at nucleation, critical and fracture.

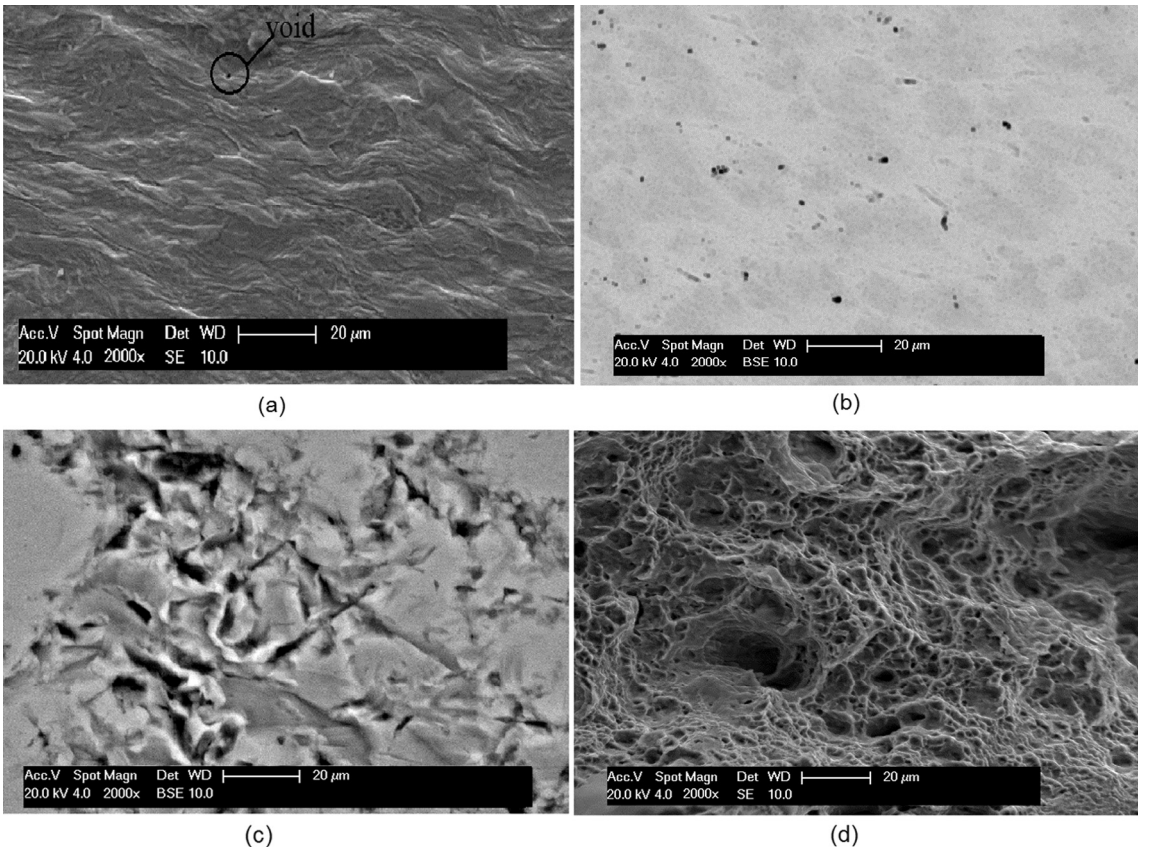

Fig. 7. Microstructure of pure titanium at different stages throughout the tensile test: (a) before deformation (initial state), (b) at void nucleation state, (c) at critical stage and (d) fracture surface.

and second-phase particles. It is difficult to predict the load where nucleation begins; therefore, the tensile test was stopped at different stages as shown in Fig. 8 in order to scan the sample to determine whether nucleation had started. In this study, nucleation started when the load reached 2.8 kN. Fig. 7(b) shows the volume fraction of the nucleated void ($f_N = 0.017$) at a nucleation strain $\varepsilon_N = 0.3$ and standard deviation $S_N = 0.1$. When the load increases and reaches the maximum value of 3.04 kN and elongation of 11 mm, significant changes in the dimensions of the tensile specimen can be noticed. Furthermore, the material's load carrying capacity is gradually lost and the void volume fraction reaches the critical value $f_c = 0.2593$ (Fig. 7 (c)). When the elongation reaches 18.8 mm, the voids become bigger and tearing of the ligaments between enlarged voids

Fig. 8. Tensile specimen under different displacements to determine the VVF at nucleation.

causes fracture in the tensile specimen. The void volume fraction at fracture is evaluated as $f_F = 0.3025$, as shown in Fig. 7(d). The damage parameters of grade 1 pure titanium are summarised in Table 2.

5.2. Influence of meshing density

Meshing density has a significant effect on predicting accurate results. A common approach is to use refined mesh with small element size in FE simulation. However, using a very small element size means that the computational time could be increased quadratically due to the increase of the total number of degrees of freedom. In FE simulation, failure prediction using the Gurson model is significantly influenced by mesh size as the model causes strain softening prior to fracture [29]. Small element size is required to capture correct deformation pattern and real shape of fracture, e.g. cup-cone failure mode [20,30]. Soyarslan et al. [31] noted the localisation band and fracture behaviour are highly dependent on mesh refinement when GTN model is used to predict the fracture with the consideration of softening material response.

In order to select the optimum mesh size to accurately predict the fracture with GTN model simulation of sheet metal, six element lengths (1.2, 1, 0.8, 0.7, 0.5 and 0.25 mm) with four layers of elements through the thickness were chosen to simulate the tensile test case as summarised in Section 5.1. The total number of elements for each mesh refinement is, as a consequence, 6923, 8594, 11,288, 13,721, 24,668 and 83,723, respectively. The ends of tensile sample were modelled as a discrete rigid to reduce the computational time and tie constraint was used to connect the discrete rigid parts with the deformable part of finer mesh. Fig. 9 shows the mesh geometry of tensile specimen with 0.5 mm element length. Abaqus element deletion technique was used to model the fracture in the sheet. A 3D hexahedral element with 8 nodes and reduced integration (C3D8R) was used to predict the fracture in the sheet with GTN model.

In this work, equivalent plastic strain distribution and force–displacement curve are used to evaluate the effect of element size. Fig. 10 shows the equivalent plastic strain distribution in the fracture zone with different mesh sizes. It is noted from the figure that with a smaller element size the increment in equivalent plastic strain can be captured earlier than that with larger element sizes. This is particularly true, when reduced integration element was chosen in FE simulation as only one integration point was used to sample strain and stress results of an element. However, as the element size is sufficiently small, FE simulation would converge to the same strain result as in the case of 0.25 mm and 0.5 mm mesh size in this study as shown in Fig. 10.

Fig. 11 shows the load-displacement curves of FE results as compared to experimental testing so as to choose a suitable mesh size for FE simulation of the studied SPIF processes using the modified GTN model. Fracture may be captured experimentally and numerically from force-displacement curve when necking occurs as the force reached its maximum and starts to drop. It is observed from the figure that the loss of load carrying capacity occurs in the model with sufficiently small element size first. This is because that the FE model with smaller element size would be able to more accurately predict the strain values and the void volume fraction (VVF) using the modified GTN models and hence the drop of load carrying capacity and the fracture of the specimen under tensile loading condition. A good correlation between the experimental and FE simulation load-displacement curves is observed for both 0.25 and 0.5 mm element sizes. Therefore, an element size of 0.5 mm was chosen in this investigation.

5.3. Validation of the modified GTN model under tensile and shear conditions

Two experimental tests (tensile and shear test) were conducted using DIC to validate the modified GTN model by comparing predicated fracture results with and without consideration of shear. As shown in Fig. 12 under tensile condition, the

Table 2
Damage parameters of pure titanium.

f_o	q_1	q_2	f_N	ε_N	S_N	f_c	f_f
0.00138	1.5	1	0.017	0.3	0.1	0.2593	0.3025

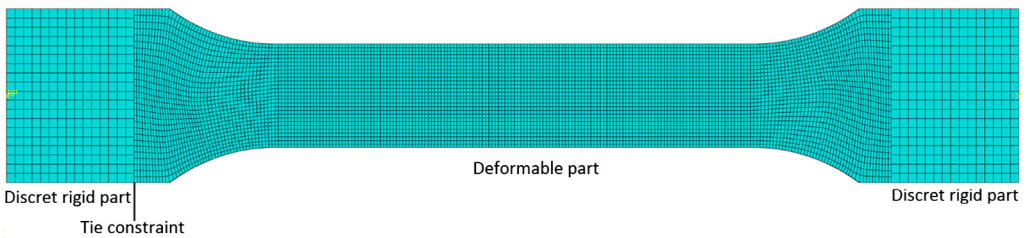

Fig. 9. FE mesh of the tensile specimen.

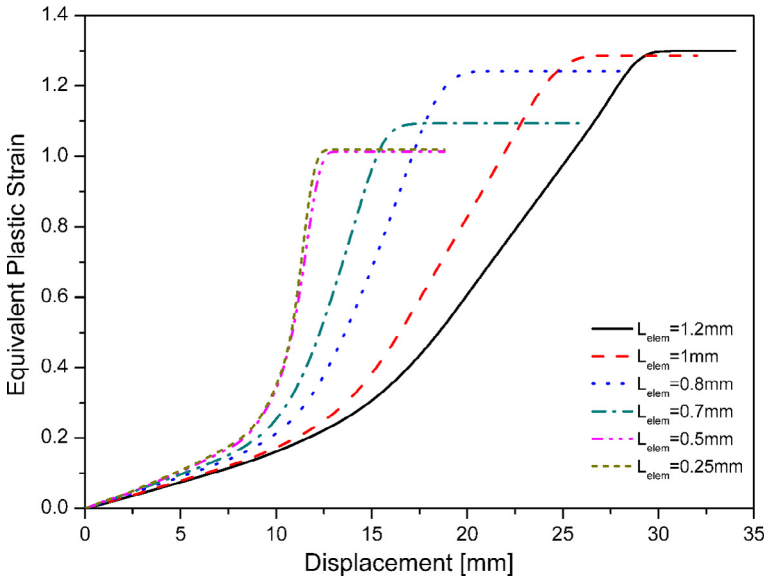

Fig. 10. Comparison of equivalent plastic strain between mesh sizes.

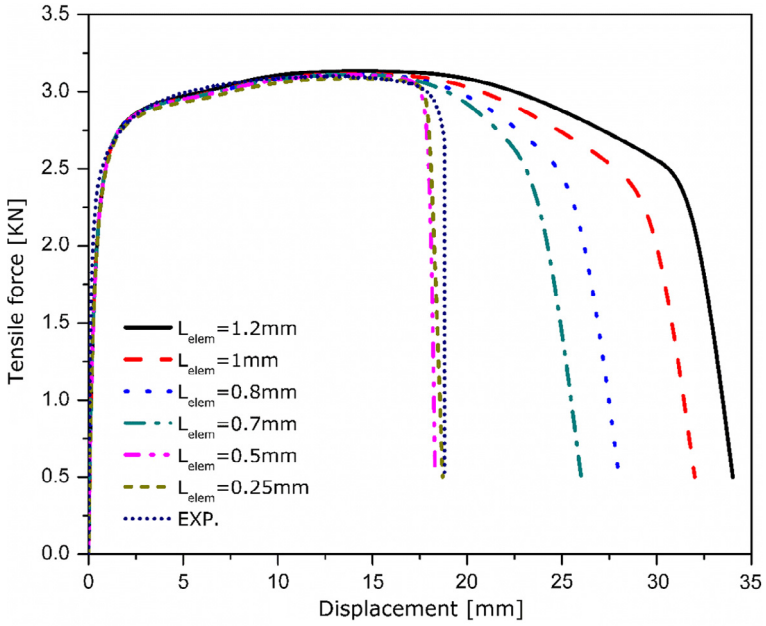

Fig. 11. Load-displacement curves with different mesh size in comparison with Experimental data.

load and displacement results showed that there was no effect of shear when comparing the experimental results with GTN models with and without considering the effect of shear.

Shear tests were also employed to validate the modified GTN model with the consideration of the shear effect to predict the fracture in the case of shear loading. Various shear sample geometries were suggested in the literature to enhance the knowledge of the material behaviour under shear, e.g. shear sample proposed by Miyauchi [32], standard shear sample (ASTM B831) [33] and twin bridge shear sample [34]. In this study the shear sample was designed according to ASTM B831 and performed on an INSTRON testing machine at strain rate of 0.00133 s^{-1}. However, through the shear tests buckling occurred in the shear zone due to the small thickness of the sample (0.7 mm) suggesting that the pure titanium with this thickness cannot resist buckling. Therefore, a modified ASTM sample [35] was used in this study as shown in Fig. 13. The modified ASTM sample was used to reduce the tendency of buckling under the effect of additional moments in the shear zone. In pure shear test the value of hydrostatic pressure is very small or zero as compared to the equivalent stress at fracture

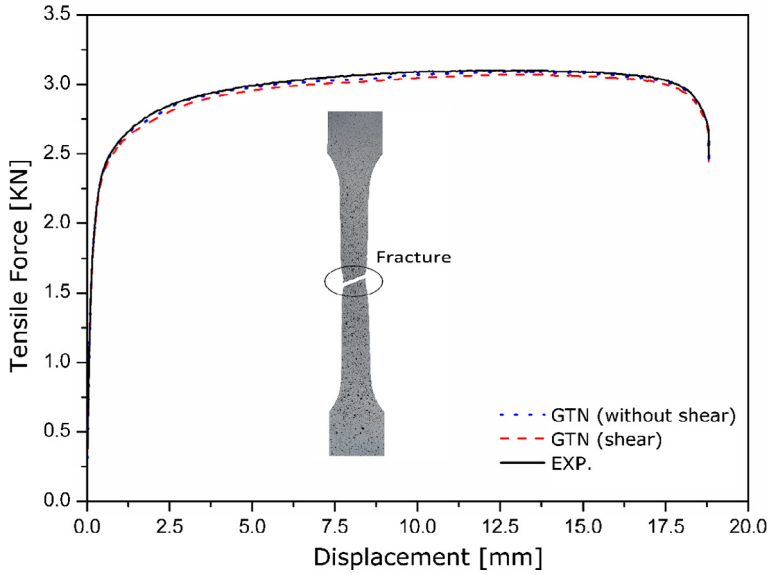

Fig. 12. Comparison of force-displacement curves of experimental tensile test with the GTN models with and without shear.

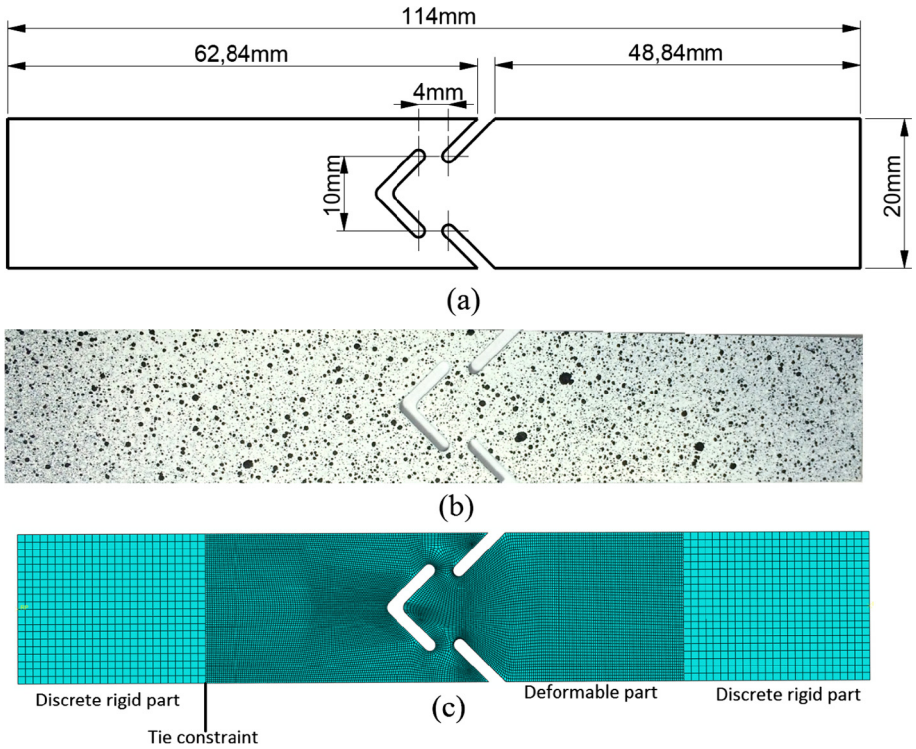

Fig. 13. Modified ASTM shear specimen: (a) specimen geometry, (b) experimental specimen and (c) meshed geometry.

zone [36]. As shown in Fig. 14, the simulated fracture is clearly seen as a direct result due to shear as the fracture line is parallel to the tensile loading. To further illustrate the suitability of the modified ASTM sample in shear testing, the stress triaxiality of the shear sample was less than 0.05 at the fracture location as compared to a value of 0.35 for standard tensile condition as shown in Fig. 15.

In this investigation, fracture is indicated from force-displacement curve where necking was considered to occur as the force reached its maximum value and started to drop. Fig. 16 shows the comparison between experimental and simulation results. Same displacement (5.3 mm) was applied on both the FE model and experimental one. It is noted from the figure that

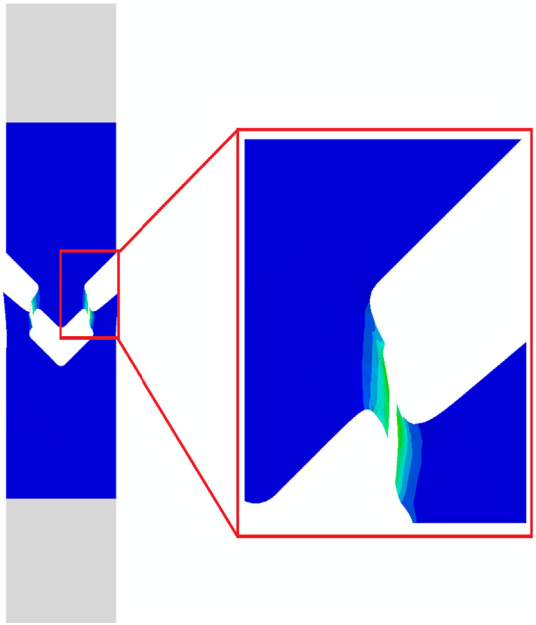

Fig. 14. Fracture shape of pure shear test (Equivalents strain distribution).

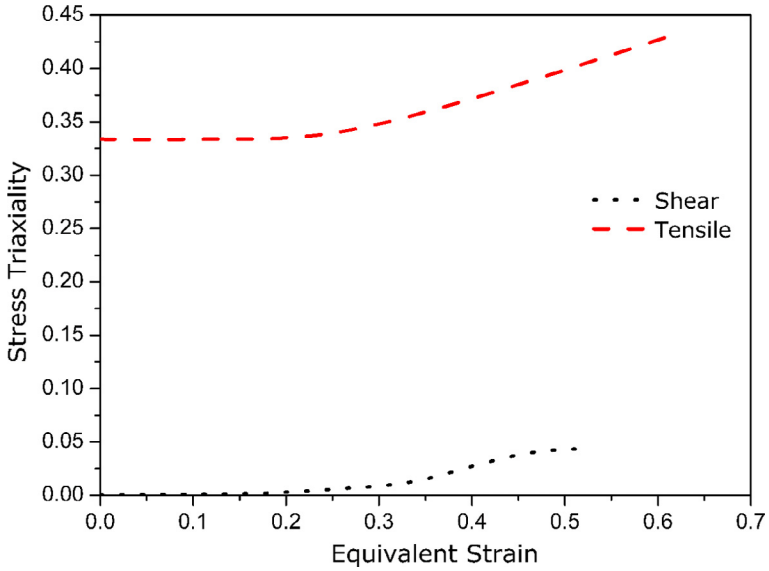

Fig. 15. Evolution of stress triaxiality for the shear and tensile test.

fracture occurs at 3.9 mm using the modified GTN model with shear effect considered and at 4.1 mm from experiment but no fracture occurs towards the end of elongation when the GTN model without shear is used. Although the modified GTN model predicts an earlier fracture by a small margin as compared to experiment, this result clearly indicates that the developed GTN model with the consideration of shear is more capable to predict fracture under shear loading conditions.

5.4. SPIF of hyperbolic cone and pyramidal shapes

As shown in Fig. 17, SPIF tests for a truncated hyperbolic conical shape and a pyramidal geometry with varying forming angles were also carried out to evaluate the fracture mechanism of both shapes under SPIF deformation conditions. These tests were carried out with an incremental depth equal to 0.2 mm per revolution and tool diameter of 10 mm. The tool is rotation free with a feed rate of 1000 mm/min for both the truncated hyperbolic cone and truncated pyramid.

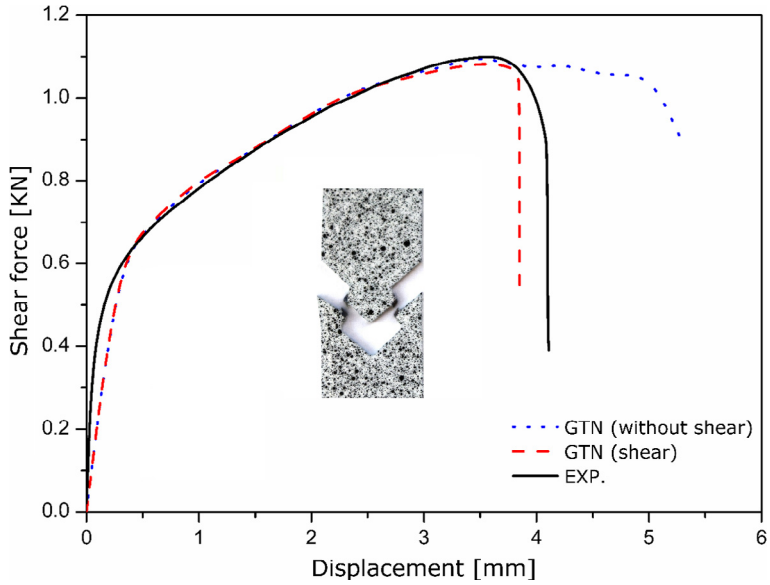

Fig. 16. Comparison of force-displacement curves of experimental shear test with GTN models with and without shear.

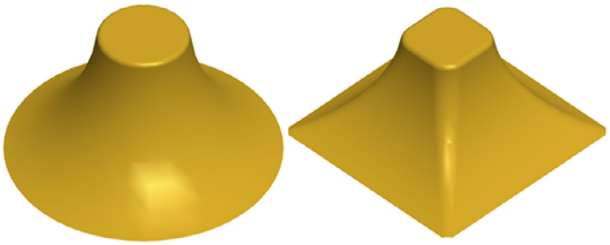

Fig. 17. Geometries require establishing FLD by using SPIF.

A hyperbolic profile was selected to test the fracture in SPIF; this part was designed with varying wall angles from 22° to 80°, as shown in Fig. 18.

Abaqus/explicit with the modified GTN model implemented through VUMAT was employed to simulate the SPIF of pure titanium sheets with dimensions 140 × 140 × 0.7 mm. In the simulation of the SPIF process, the tool, backing plate and the blankholder were modelled as an analytical rigid surface. The blank was modelled as a deformable body with an eight node brick element (C3D8R). Velocity vs time was used to define the tool path in SPIF. The element size is 0.5 mm with three layers

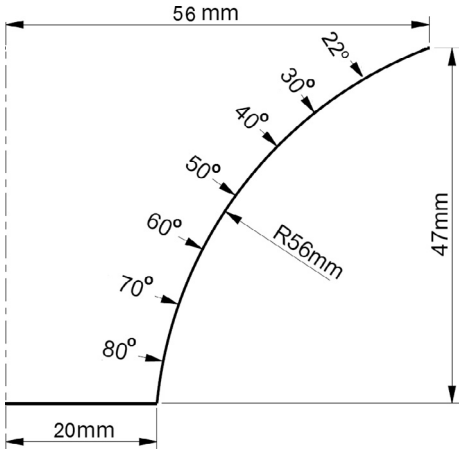

Fig. 18. Geometric shape of hyperbolic profile.

through the thickness. The total number of elements in the SPIF model is 235,200 elements. Coulomb's friction law was applied with a friction coefficient of 0.1 to the contact surface between the forming tool and the blank. To save computation time, mass scaling techniques have been widely employed; however, these techniques can yield poor results if a large scaling factor is used due to the increase in dynamic effects. Typically, the kinetic energy should remain less than 4–10% of the internal energy for the whole model. In Abaqus/explicit, two types of mass scaling options, i.e. fixed and variable may be used. In this work, the variable mass scaling is selected as it is most useful when the stiffness properties that control the stable time increment change significantly during each step.

Unfortunately, no threshold is given to decide how much scaling is permissible. Therefore, three stable time increments ($\Delta t = 2 \times 10^{-4}$, 2×10^{-5}, and 2×10^{-6} s) were chosen to identify which one would provide acceptable accuracy as compared to the desired geometry, with relative values between Kinetic and Internal energy less than 4–10%. Fig. 19 shows the history of the dynamic energy with different stable time increments. It can be seen clearly that, with stable time increments of 2×10^{-4} s and 2×10^{-5} s, the kinetic energy exceeded 10% of the internal energy, while with another stable time increment (2×10^{-6} s), the relative values of energy are less than 4%. Therefore, the FE simulation of SPIF was run on a high performance computing (HPC) system using 48-core. The required time to complete the simulation with mass scaling was approximately 120 h.

Since the modified GTN model was used to predict the fracture occurrence in the FE simulation, it is important to investigate the distribution of VVF on the part during deformation. Fig. 20 shows the distribution of VVF obtained by FE simulation along the achievable depth. It is noted from the figure that the value of initial VVF before deformation was 0.00138 (Fig. 20 (a)) and it is increased when the tool moves down along the defined tool path. The highest values of VVF are always in the transition area between contact and noncontact zones in the outside of the wall. It can be concluded that the voids are nucleated only in the tension state. Moreover, in the transition area, maximum thinning occurs and this is considered as a factor to predict the tearing by FE simulation, so the sheet thinning leads to increased VVF due to an increase in stretching by meridional stress. In the FE simulation, the distribution of VVF is almost uniform in the early stages of the SPIF process and it tends to localise during the process. The VVF accumulation leads to sudden fracture in the part when its value reaches 0.3025, as shown in Fig. 20(e and f).

In order to evaluate the void volume fraction and major strain in the sheet after fracture, five neighbouring elements were selected, one of which was in the fracture (unsafe zone) and others on one side of the fracture (safe zone) as shown in Fig. 21. Fig. 22 compares the evolution of the VVF. As can be seen in the figure, in the early deformation stages, the VVF grows uniformly until 118 s when these curves begin to separate from each other and increase rapidly over a short period. This means that the VVF starts to grow when the stretching in the wall increases and reaches a certain value. However, the value of the VVF in element A is equal to or more than the final value of the VVF (0.3025), which is determined experimentally by SEM, so this element is deleted from the FE model, as shown in Fig. 21. Element B is located in the critical zone with a VVF value of 0.22, which is close to the critical experimental value (0.2593). The other elements (C, D and E) remain in the safe zone and their VVF values are well below the critical value.

Major strain is commonly used as a criterion to detect the onset of fracture in the sheet metal forming process. Fig. 23 shows the growth of major strains with the time of the same elements used to evaluate the VVF. It is evident from the figure that the distribution of major strain shows the same trend as the VVF distribution.

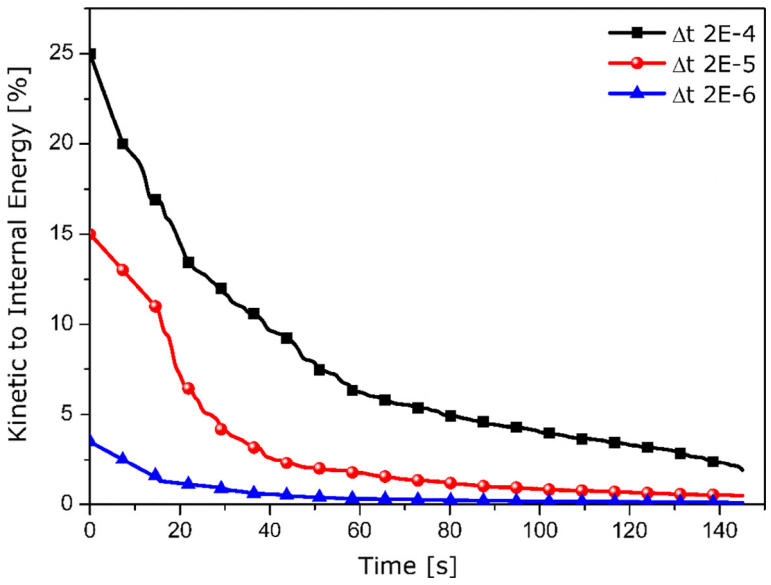

Fig. 19. The ratio between kinetic and internal energy for the ISF process.

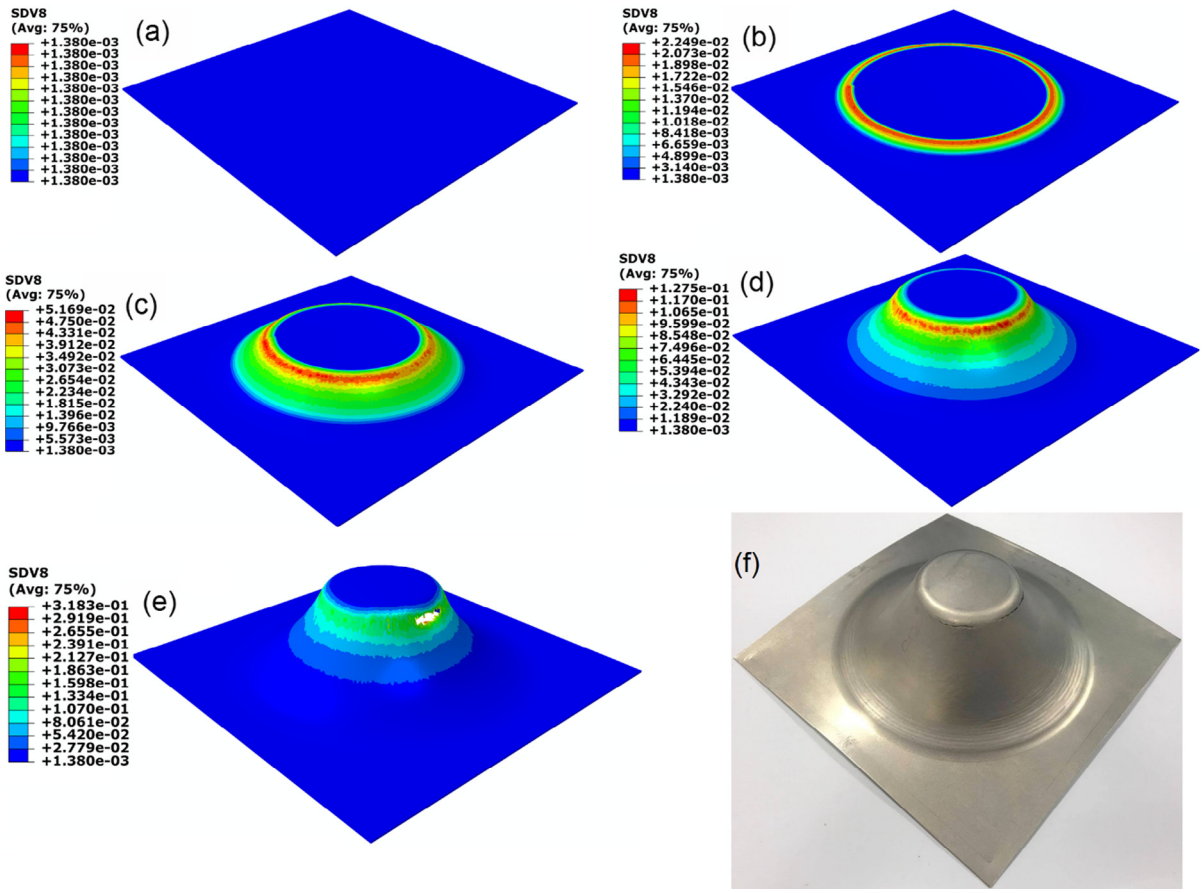

Fig. 20. Distribution of the void volume fraction obtained by numerical simulation of a SPIF process with different depths.

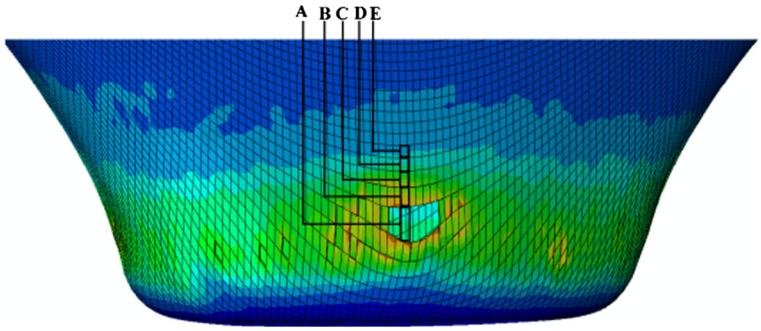

Fig. 21. Location of selected elements on the FE model.

Nahshon-Hutchinson's shear mechanism is used in the present work to study the effect of shear on the fracture in SPIF. Two jobs were run with one using the original GTN model (porous metal plasticity model Mises-GTN/Explicit) and the other using the modified GTN model via the VUMAT subroutine. Fig. 24 represents a comparative illustration of the effect of the shear mechanism on the VVF growth during SPIF. It is evident from the figure that the VVF reaches the fracture value earlier by using the modified GTN model with shear than that without consideration of shear, which indicates that the shear mechanism accelerates fracture occurrence in SPIF.

To validate the results obtained from the original GTN model and modified GTN model with consideration of shear, the FE results were compared with experimental work, as shown in Fig. 25. To ensure the repeatability of the results, the experimental test of SPIF process was repeated three times and the average value is taken. The SPIF simulated results with shear

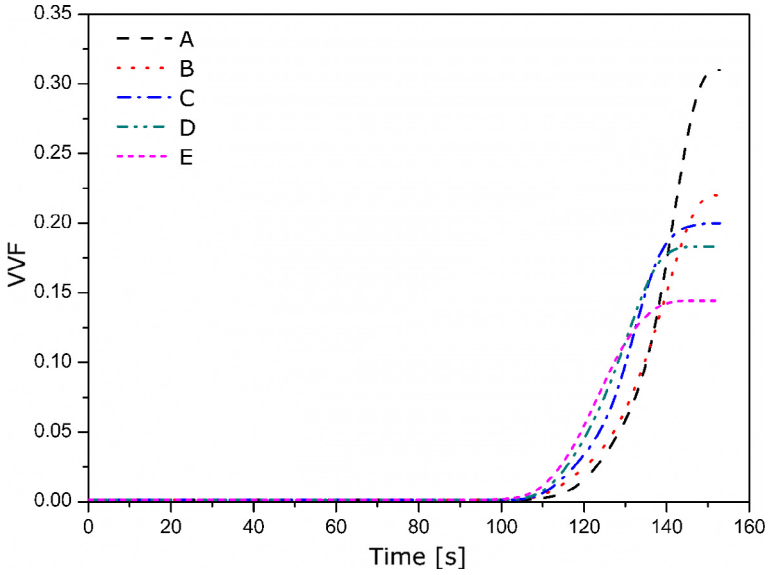

Fig. 22. Evolution of voids during the SPIF process.

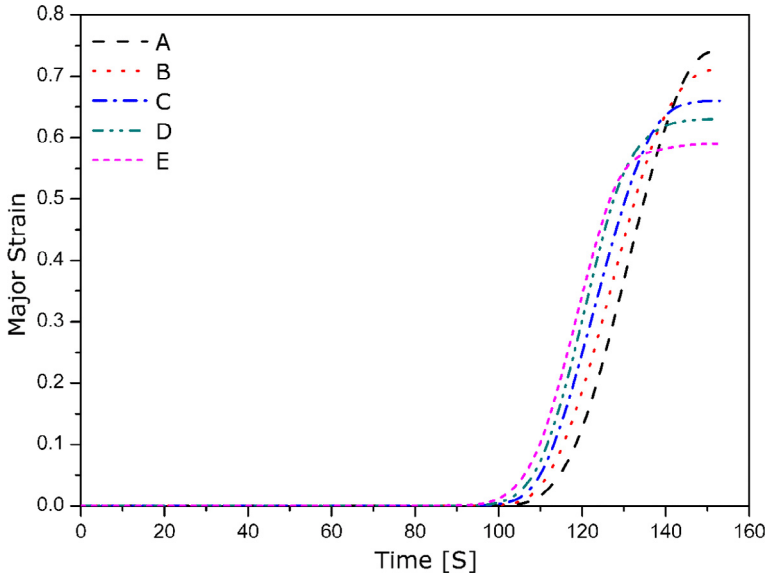

Fig. 23. Evolution of major strain during the SPIF process.

consideration were consistent with experiments suggesting that the modified GTN model is capable of capturing the fracture in SPIF.

For the case of the pyramidal shape, the same GTN model parameters and SPIF procedure were used as the hyperbolic shape. The reason of making two different shapes is to study the ability of the modified GTN model to predict fracture at different strain states from two different shapes. In particular, with the hyperbolic conical shape the plane strain stretching is created but with the pyramidal shape both plane strain and biaxial strain stretching are present.

Fig. 26 shows the predicted VVF values of both GTN models with and without shear. It is clear from the figure that the fracture occurs earlier with the consideration of shear and it is closer to the experimental result. It can be concluded that the shear clearly plays a role in the stretching along the meridional direction to develop the fracture in SPIF.

As shown in Fig. 27, the fracture occurred at the corner area of a depth of 28.64 mm and 25.5 mm from the original and modified GTN models as comparted to a depth of 26.7 mm from experimental testing. The FE result of the shear modified GTN model was in a good agreement with experiments. The fracture is developed in the corner area due to biaxial stretching deformation as compared to a plane strain stretching along the straight side.

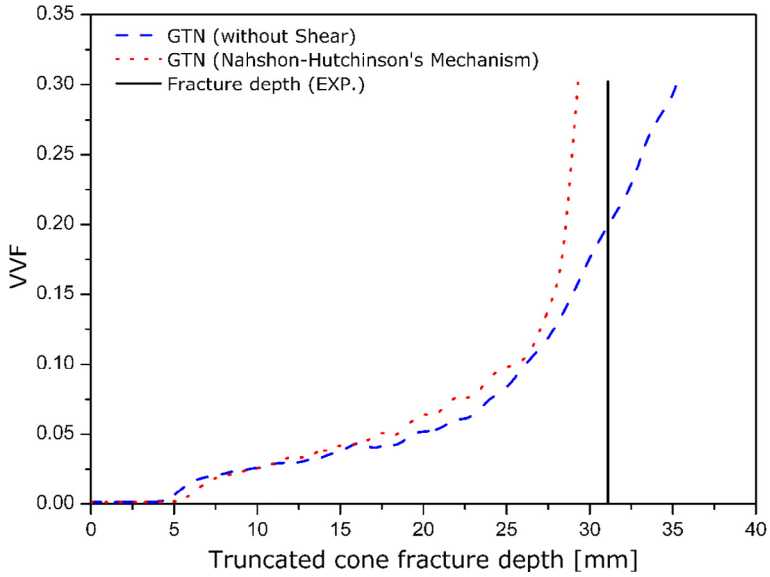

Fig. 24. Comparison between GTN models with and without shear of the hyperbolic shape.

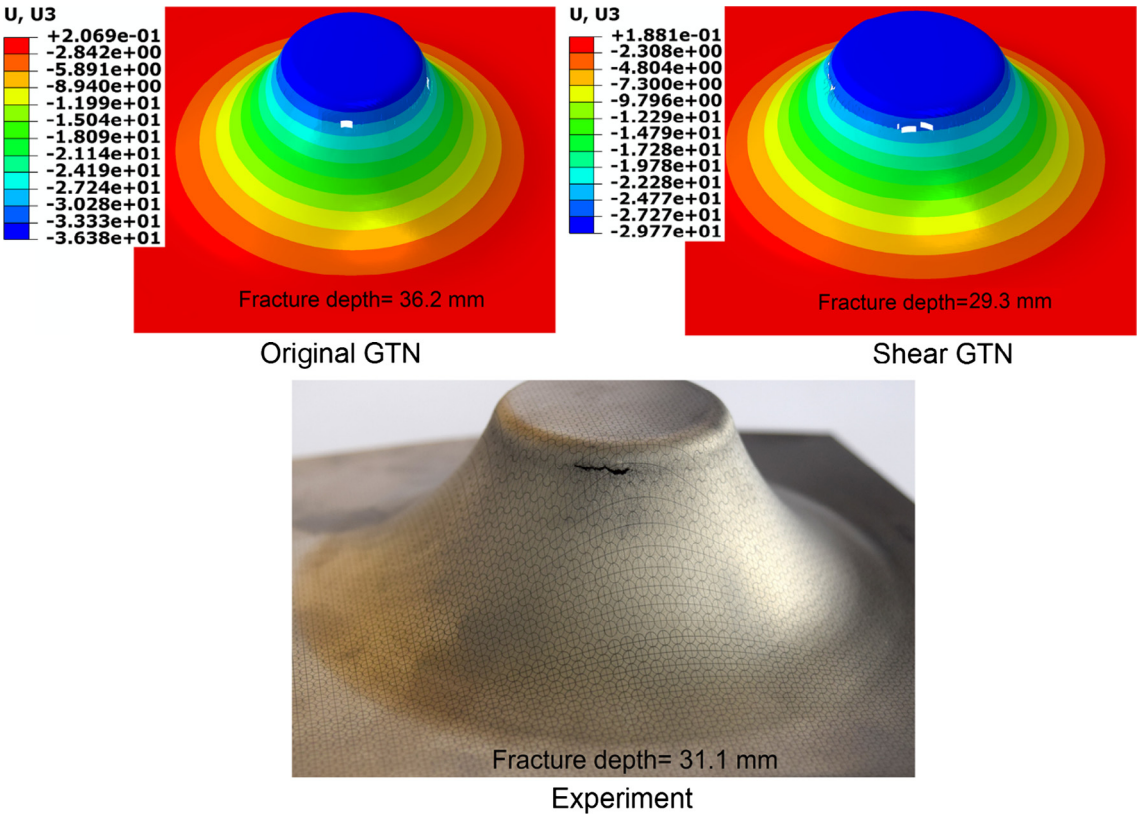

Fig. 25. Simulated results from the original and modified GTN model in comparison with actual experiment of the hyperbolic shape.

From SPIF tests of both shapes, the hyperbolic shape can perform a higher forming angle than the pyramidal shape. The maximum wall angle of the hyperbolic conical shape at fracture was 68.4° and the pyramidal shape achieved a maximum wall angle of 61.2°. This suggests that fracture in SPIF is also dependent upon the stress states (stress triaxiality ratio).

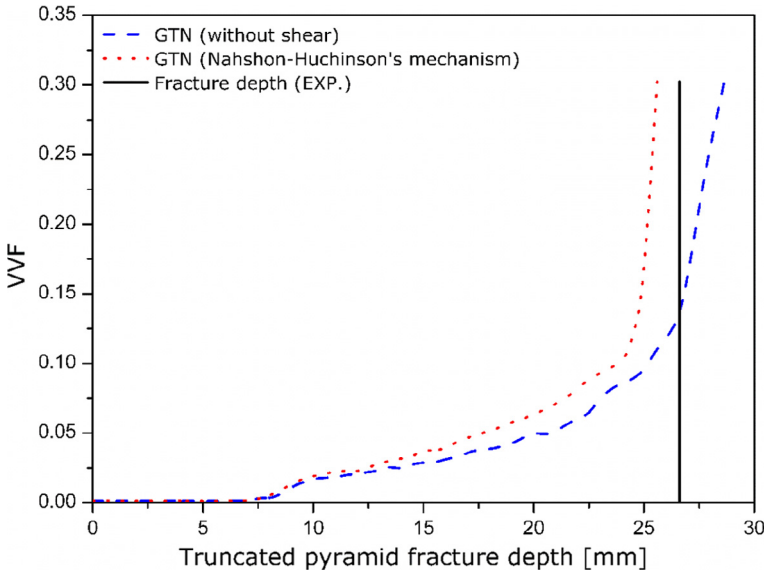

Fig. 26. Comparison between GTN models with and without shear of the truncated pyramid.

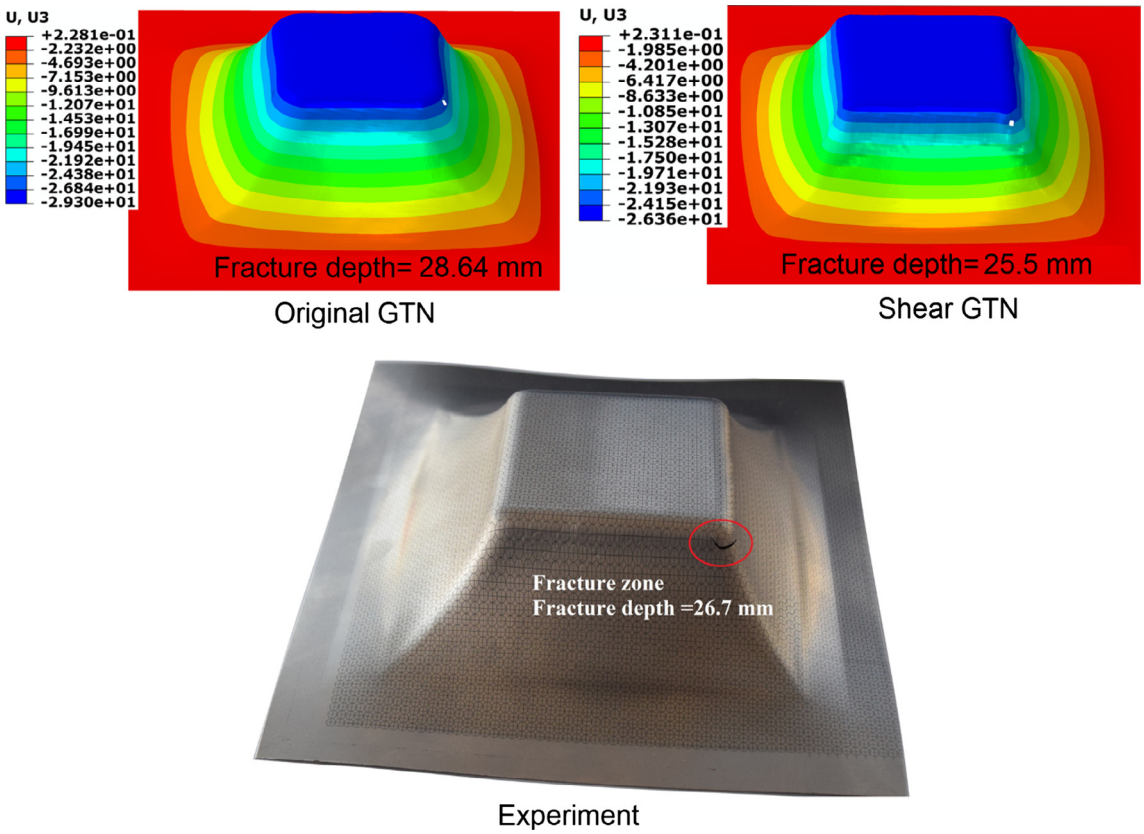

Fig. 27. Simulated results from the original and shear modified GTN model in comparison with actual experiment of the truncated pyramid.

The formability (maximum wall angle) of SPIF can be altered with the stress triaxiality ratio, higher wall angle can be achieved with low stress triaxiality ratio as compared to high stress triaxiality ratio. Due to the fact that the hyperbolic truncated cone deforms under plane strain condition and the hyperbolic truncated pyramid deforms under plane strain and equi-

biaxial strain conditions and the ratio of stress triaxiality at plane strain condition is lower than that at equi-biaxial strain. Therefore, high wall angle can be achieved with hyperbolic truncated cone as compared to hyperbolic truncated pyramid.

6. Conclusions

A modified GTN model was developed to comprehensively study fracture in SPIF with a specific attention to the effect of shear for the first time by using a combined approach of experimental testing for GTN parameters and SPIF testing for FE results validation. The following conclusions may be drawn from this study:

- DIC system was used to analyse and evaluate the necking and instability along the tensile specimen, and SEM was utilised to scan the affected zone of the tensile specimen to determine the parameters of the modified GTN model experimentally. Based on the results obtained, the DIC and SEM are considered an effective means to derive the modified GTN model parameters.
- Fracture prediction using GTN model is significantly influenced by mesh density, i.e., sufficiently small element size is required to capture the correct deformation pattern and real shape of fracture.
- To determine the ability of the modified GTN model to predict the damage under shear loading, two experimental tests (tensile and shear test) were conducted with DIC. The results showed that the modified GTN model with shear improved the modelling accuracy of fracture over the original GTN model under shear loading conditions.
- The experimental results of SPIF processing for truncated hyperbolic cone and truncated pyramid showed a good agreement on the occurrence of fracture for both shapes with the modified GTN model. This clearly shows that shear plays a role with meridional tensile stress to accelerate damage in SPIF processes
- Further work is needed to investigate the effect of stress triaxiality to the fracture occurrences as the Nahshon-Hutchinson based shear model can predict the fracture at low stress triaxiality.

Acknowledgements

This work was supported by the Engineering and Physical Science Research Council [grant number EP/L02084X/1]; and the International Research Staff Exchange Scheme [IRSES, MatProFuture project, 318,968] within the 7th European Community Framework Programme (FP7).

References

[1] Martins PAF, Bay N, Skjoedt M, Silva MB. Theory of single point incremental forming. CIRP Ann – Manuf Technol 2008;57(1):247–52.
[2] Silva MB, Skjoedt M, Martins PAF, Bay N. Revisiting the fundamentals of single point incremental forming by means of membrane analysis. Int J Mach Tools Manuf 2008;48:73–83.
[3] Decultot N, Robert L, Velay V, Bernhart G. Single point incremental sheet forming investigated by in-process 3D digital image correlation. EPJ Web Conf 2010;6:11001.
[4] Malhotra R, Xue L, Cao J, Belytschko T. Identification of deformation mechanisms responsible for failure in incremental forming using a damage based fracture model. In: AIP conference proceedings. AIP; 2011.
[5] Malhotra R, Xue L, Belytschko T, Cao J. Mechanics of fracture in single point incremental forming. J Mater Process Technol 2012;212(7):1573–90.
[6] Xu D, Malhotra R, Chen J, Lu B, Cao J. Numerical and experimental studies for the effects of through-the-thickness shear on formability in single point incremental forming. In: AIP conference proceedings. AIP; 2013.
[7] Allwood J, Shouler D, Tekkaya AE. The increased forming limits of incremental sheet forming processes. In: Key engineering materials. Trans Tech Publ; 2007.
[8] Emmens W, Boogaard A, Weijde D. The FLC, enhanced fromavbility, and incremental sheet forming; 2009.
[9] Jackson K, Allwood J. The mechanics of incremental sheet forming. J Mater Process Technol 2009;209(3):1158–74.
[10] Cao TS, Montmitonnet P, Bouchard PO. A detailed description of the Gurson–Tvergaard–Needleman model within a mixed velocity–pressure finite element formulation. Int J Numer Meth Eng 2013;96(9):561–83.
[11] Isik K, Gerstein G, Clausmeyer T, Nürnberger F, Tekkaya AE, Maier HJ. Evaluation of void nucleation and development during plastic deformation of dual-phase steel DP600. Steel Res Int 2016;87:1–9.
[12] Chen Z, Dong X. The GTN damage model based on Hill'48 anisotropic yield criterion and its application in sheet metal forming. Comput Mater Sci 2009;44(3):1013–21.
[13] Kami A, Mollaei Dariani B, Sadough Vanini A, Comsa DS, Banabic D. Application of a GTN damage model to predict the fracture of metallic sheets subjected to deep-drawing. In: Proceedings of the Romanian Academy, Series A; 2014, vol. 15, p. 300–9.
[14] Kami A, Dariani BM, Vanini AS, Comsa DS, Banabic D. Numerical determination of the forming limit curves of anisotropic sheet metals using GTN damage model. J Mater Process Technol 2015;216:472–83.
[15] Lievers WB, Pilkey AK, Lloyd DJ. Using incremental forming to calibrate a void nucleation model for automotive aluminum sheet alloys. Acta Mater 2004;52(10):3001–7.
[16] Smith J, Malhotra R, Liu W, Cao J. Application of a shear-modified GTN model to incremental sheet forming. In: AIP conference proceedings. AIP; 2013.
[17] Gurson AL. Continuum theory of ductile rupture by void nucleation and growth: Part I—Yield criteria and flow rules for porous ductile media. J Engng Mater Technol 1977;99(1):2–15.
[18] Batista RG, Iturrioz I, Cisilino AP. Computational modelling of the micromechanics of void growth and coalescence in ductile failure via the Discrete Element Method. Solid Mech Brazil 2007:97.
[19] Kossakowski PG, Trampczynski W. Microvoids evolution in S235JR steel subjected to multi-axial stress state. Eng Trans 2012;60(4):287–314.
[20] Tvergaard V, Needleman A. Analysis of the cup-cone fracture in a round tensile bar. Acta Metall 1984;32(1):157–69.
[21] SIMULIA, ABAQUS 6.16, Analysis User's Manual; 2016.
[22] Xue L. Constitutive modeling of void shearing effect in ductile fracture of porous materials. Eng Fract Mech 2008;75(11):3343–66.
[23] Aravas N. On the numerical integration of a class of pressure-dependent plasticity models. Int J Numer Meth Eng 1987;24(7):1395–416.

[24] Tvergaard V. Influence of void nucleation on ductile shear fracture at a free surface. J Mech Phys Solids 1982;30(6):399–425.
[25] Nahshon K, Hutchinson J. Modification of the Gurson model for shear failure. Eur J Mech – A/Solids 2008;27(1):1–17.
[26] Reis F, Malcher L, Andrade Pires F, César de Sá J. A comparison of shear mechanisms for the prediction of ductile failure under low stress triaxiality. Int J Struct Integr 2010;1(4):314–31.
[27] Ortiz M, Simo J. An analysis of a new class of integration algorithms for elastoplastic constitutive relations. Int J Numer Meth Eng 1986;23(3):353–66.
[28] Engelmann BE, Whirley RG. Recent developments in NIKE2D for metalforming analysis and low rate impact. Nucl Eng Des 1992;138(1):23–35.
[29] Hooputra H, Gese H, Dell H, Werner H. A comprehensive failure model for crashworthiness simulation of aluminium extrusions. Int J Crashworth 2004;9(5):449–64.
[30] Becker R, Needleman A. Effect of yield surface curvature on necking and failure in porous plastic solids. J Appl Mech 1986;53(3):491–9.
[31] Soyarslan C, Gharbi MM, Tekkaya A. A combined experimental–numerical investigation of ductile fracture in bending of a class of ferritic–martensitic steel. Int J Solids Struct 2012;49(13):1608–26.
[32] Miyauchi K. A proposal for a planar simple shear test in sheet metals. Sci Pap Inst Phys Chem Res (Jpn) 1984;78(3):27–40.
[33] ASTM international B 831-05. Standard test method for shear testing of thin aluminum alloy products. West Conshohocken, USA; 2005.
[34] Brosius A, Yin Q, Güner A, Tekkaya A. A new shear test for sheet metal characterization. Steel Res Int 2011;82(4):323–8.
[35] Isik K, Silva MB, Tekkaya AE, Martins PAF. Formability limits by fracture in sheet metal forming. J Mater Process Technol 2014;214(8):1557–65.
[36] Bao Y, Wierzbicki T. On fracture locus in the equivalent strain and stress triaxiality space. Int J Mech Sci 2004;46(1):81–98.